Drift-based scrape-off particle width in X-point geometry

D. Reiser¹ and T. Eich²

The Goldston heuristic estimate of the scrape-off layer width (Nucl. Fusion 52, 013009, 2012) is reconsidered using a fluid description for the plasma dynamics. The basic ingredient is the inclusion of a compressible diamagnetic drift for the particle cross field transport. Instead of testing the heuristic model in a sophisticated numerical simulation including several physical mechanisms working together, the purpose of this work is to point out basic consequences for a drift-dominated cross field transport using a reduced fluid model. To evaluate the model equations and prepare them for subsequent numerical solution a specific analytical model for 2D magnetic field configurations with X-points is employed. In a first step parameter scans in high-resolution grids for isothermal plasmas are done to assess the basic formulas of the heuristic model with respect to the functional dependence of the scrape-off width on the poloidal magnetic field and plasma temperature. Particular features in the 2D-fluid calculations - especially the appearance of supersonic parallel flows and shock wave like bifurcational jumps - are discussed and can be understood partly in the framework of a reduced 1D model. The resulting semi-analytical findings might give hints for experimental proof and implementation in more elaborated fluid simulations.

I. INTRODUCTION

The heuristic model of Goldston [1] has attracted much interest and discussion in the studies of scrape-off layer power width and has been compared with several experimental results [2; 3]. However, its analytical framework does not take into account several details of the magnetic field shaping, parallel flow balances, electric fields and neutral physics. The purpose of this contribution is to complement the heuristic estimate of Goldston and to assess the particular implications of the drift-based radial particle transport for the scrape-off layer (SOL) width in an axisymmetric tokamak geometry including an X-point. The basic ideas of Goldston's approach are rewritten as a reduced 2D fluid model taking into account particle balance and parallel momentum balance in an isothermal plasma. The basic ingredient is the inclusion of a compressible diamagnetic drift for the particle cross field transport. Numerical solution of this reduced transport model shows that

- (1) the specifics of the drift-based radial transport introduces particle and momentum sinks in the SOL dynamics causing supersonic flows contrary to diffusive seeding of the SOL.
- (2) in standard ASDEX Upgrade geometry and in case that particle transport is determined by electron diamagnetic drift the SOL width is often well approximated by a constant decay length Λ , characterizing an exponential decay of particle density with respect to the flux label coordinate.
- (3) for radial particle flows dominated by the ion diamagnetic drift a globally constant decay length is not established for the standard ASDEX Upgrade configuration and parallel flows exhibit shock wave like signatures with strong gradients in density and Mach number.
- (4) the basic dependencies of SOL width on the poloidal Larmor radius remain unchanged in X-point geometries.

In the cases where an almost constant density decay length is found the reduction to a 1D model is justified and it is shown that the resulting semi-analytical predictions reproduce quite well the findings of the 2D simulations, in particular the supersonic transitions. Moreover, it offers an alternative derivation for Goldston's estimate and can be extended easily to an estimate including additional particle diffusion, therefore giving boundaries for detailed studies of the drift-based transport with more sophisticated fluid simulations, e. g. a study with first results on more detailed modelling of drift effects closely related to the considerations in this work published recently [4].

The paper is structured as follows: In Section II the basic equations of the 2D fluid model are presented and in Section III the model tokamak geometry for the numerical simulations are elucidated. Results for the density profiles and flow velocities obtained by numerical solution of the 2D model in the electron drift dominated regime are presented and discussed in Section IV. Justified by these 2D results a 1D model reduction is derived and presented in Section V. In Section VI the ion-drift dominated regime is considered and its significant discrepancies to the results of Section IV are discussed. In Section VII further results from 2D simulations for varying plasma parameters are presented and compared with the predictions of the reduced 1D model. In Section VIII also the effect of an additional diffusive particle transport is analysed on the basis of 2D simulations and a simple extension of the 1D model as well. The concluding Section IX summarizes the results of this paper.

II. FLUID FORMULATION OF GOLDSTON'S HEURISTIC MODEL

To study the consequences of Goldston's ideas on the drift-based SOL width in a tokamak geometry with X-

¹Forschungszentrum Jülich GmbH, Institut für Energie- und Klimaforschung – Plasmaphysik, Partner of the Trilateral Euregio Cluster (TEC), 52425 Jülich, Germany

²Max-Planck-Institut für Plasmaphysik, Boltzmannstr. 2, 85748 Garching, Germany

point and asymmetrical shaping a simplified model is considered translating the ideas of the heuristic model presented in [1] to a 2D fluid picture for the plasma dynamics. In this first stage the model consists of the balance equations for particles and parallel ion momentum. The electron and ion temperatures are assumed to be equal and prescribed. Parallel currents are neglected, i.e. $u_{\parallel}=v_{\parallel}$, where u_{\parallel} is the parallel ion flow velocity and v_{\parallel} the parallel electron velocity. The model equations for the particle density n and the velocity u_{\parallel} in a SOL without particle and momentum sources read

$$\frac{\partial n}{\partial t} + \nabla \cdot (n\mathbf{u}_{\parallel}) \pm \nabla \cdot (n\mathbf{u}_{*}) = 0 \tag{1}$$

$$\frac{\partial}{\partial t} \left(n u_{\parallel} \right) + \boldsymbol{\nabla} \cdot \left(n \mathbf{u}_{\parallel} u_{\parallel} \right) = -\frac{2 \nabla_{\parallel} p}{m_{i}} \tag{2}$$

where

$$\mathbf{u}_* = \frac{\mathbf{B} \times \nabla p}{enB^2} \tag{3}$$

denotes the ion diamagnetic drift and u_{\parallel} is the parallel ion velocity. The divergence of the diamagnetic particle flux can be rewritten due to the following relation

$$\nabla \cdot (n\mathbf{u}_*) = \nabla \cdot \left(\frac{\mathbf{B} \times \nabla p}{eB^2}\right) = \nabla \cdot (n\mathbf{u}_{\times}) = \mathbf{u}_{\times} \cdot \frac{\nabla p}{T}$$
 (4)

The velocity \mathbf{u}_{\times} is given as

$$\mathbf{u}_{\times} = \frac{T}{e} \, \mathbf{\nabla} \times \frac{\mathbf{B}}{B^2} = \frac{2T}{eB} \, \frac{\mathbf{B} \times \mathbf{\nabla} B}{B^2} + \frac{T}{e} \, \frac{\mathbf{\nabla} \times \mathbf{B}}{B^2} \tag{5}$$

and is representing the particle guiding center drifts in an inhomogeneous magnetic field [5; 6]. This particular relation between the ∇B -guiding center drift and the fluid diamagnetic drift is discussed in detail in Sec. 4.5 of the monograph of Hazeltine and Meiss [7]. On the one hand the Eqs. 1 and 2 considered here define an exercise to study the signature of perpendicular particle flow dominated by diamagnetic effects as discussed by Goldston. But it is important to note that the corresponding diamagnetic currents immediately opens the discussion on the meaning of these approximations with respect to the underlying distribution of current density \mathbf{J} with repsect to the requirement of quasineutrality, i. e. $\nabla \cdot \mathbf{J} = 0$. To retain readability of the text a more detailed consideration of this issue has been put into Appendix A. Here we just confine ourselves to the brief comment that we assume that either the electron or the ion diamagnetic drift dominate the particle transport and other contributions due to parallel currents, electric fields, viscous drifts and sources cancel out. Of course, this limits the range of validity of the proposed model. In particular particle sources as a consequence, e. g. from strong recycling might change the results strongly. However, the intention of this work is to extract the signatures of a transport based on diamagnetic drift effects and postponing extensions to future work. Therefore, following the discussions in [1] and in Appendix A of this work we refer these distinct scenarios as electron-diamagnetic-drift regime (EDD-regime) and ion-diamagnetic-drift regime (IDD-regime). Due to the assumption of equal electron and ion temperature used here the diamagnetic electron drift \mathbf{v}_* is just the $-\mathbf{u}_*$, the ion diamagnetic drift with opposite sign. and therefore, choosing the plus-sign in Eq. 1 means that the perpendicular particle transport is driven by the ion magnetic drift, whereas the minus-sign means that an electron drift dominated regime is considered.

III. MODEL MAGNETIC FIELD CONFIGURATION

An axisymmetric magnetic field **B** is described in righthanded orthogonal coordinates (r, θ, ϕ) by

$$\mathbf{B} = B^{\theta} \,\mathbf{e}_{\theta} + B^{\phi} \,\mathbf{e}_{\phi} \tag{6}$$

The coordinate r is a flux label. For a divergence free field, i. e.

$$\nabla \cdot \mathbf{B} = \frac{1}{J} \frac{\partial}{\partial \theta} \left(J B^{\theta} \right) = 0 \tag{7}$$

the poloidal contravariant component B^{θ} must be of the form

$$B^{\theta} = \frac{B_0 C}{I} \tag{8}$$

where C = C(r) is a flux label too, B_0 is a constant and $J = \mathbf{e}_r \cdot \mathbf{e}_\theta \times \mathbf{e}_\phi$ is the Jacobian. The function C(r) is directly related to the plasma current I_p and can be chosen by requiring a particular value for the flux surface averaged physical poloidal field $\langle \hat{B}_\theta \rangle$ at the separatrix according to an experimental setup and using the approximate formula

$$\langle \hat{B}_{\theta} \rangle = \frac{\mu_0 I_p}{2\pi a \sqrt{(1 + \kappa^2)/2}} \tag{9}$$

where a is the minor radius and κ denotes the elongation [9]. The toroidal contravariant component is chosen in a tokamak like form

$$B^{\phi} = \frac{B_0 R_0}{R^2} \tag{10}$$

where the functional relation for R as a function of r and θ is given in the Appendix B by Eq. B2. The detailed definition of the coordinates (r, θ, ϕ) based on a conformal map is also presented in Appendix B. The explicit form of the model equations Eqs. 1-2 for these coordinates is

$$\frac{\partial n}{\partial t} + \frac{1}{J} \frac{\partial}{\partial \theta} \left(J \frac{B^{\theta}}{B} n u_{\parallel} \pm J n u_{\times}^{\theta} \right) \pm \frac{1}{J} \frac{\partial}{\partial r} \left(J n u_{\times}^{r} \right) = 0 \quad (11)$$

$$\frac{\partial}{\partial t} \left(m_i n u_{\parallel} \right) + \frac{1}{J} \frac{\partial}{\partial \theta} \left(J \frac{B^{\theta}}{B} m_i n u_{\parallel}^2 \right) = -\frac{2B^{\theta}}{B} \frac{\partial p}{\partial \theta} \tag{12}$$

where the contravariant components of \mathbf{u}_{\times} are

$$u_{\times}^{r} = -\frac{2T}{eB} \frac{B_{\phi}}{JB^{2}} \frac{\partial B}{\partial \theta}, \quad u_{\times}^{\theta} = \frac{2T}{eB} \frac{B_{\phi}}{JB^{2}} \frac{\partial B}{\partial r},$$
 (13)

The magnetic field geometry considered in this work is sketched in Fig. 1 left, and profiles of the physical radial component \mathbf{u}_{\times} for this configuration are shown in Fig. 2 and in Fig. 3 top.

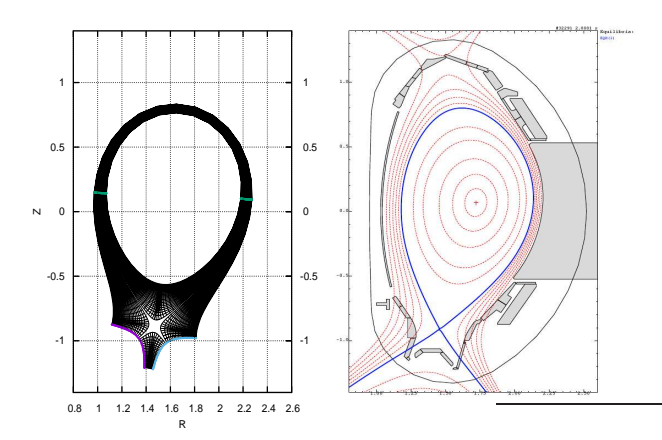


FIG. 1 (Color online) Model geometry for ASDEX like magnetic field based on the conformal mapping presented in the Appendix B. On the left the computational domain is shown for R_0 =1.65 m, h=1.2 m and rotation angle ξ =-0.15 (with a smaller number of grid points than used in the computations for better visibility). The points in red label the inner target (θ =-0.7), the points in blue the outer target (θ =6.98). The separatrix is located at r=h and $0 \le \theta \le 2\pi$. The X-point is located at θ =0 and θ =2 π , respectively. The right figure shows the equilibrium reconstruction of ASDEX Upgrade shot No. 32291 at t=2 s serving as a template for the conformal map in the left figure.

IV. 2D SIMULATIONS IN X-POINT GEOMETRY FOR ELECTRON DIAMAGNETIC DRIFT DOMINATED TRANSPORT

At first we study the regime dominated by the electron diamagnetic drift (denoted by EDD-regime in Appendix A). The model equations Eqs. 11 (with minussign) and 12 are solved numerically on orthogonal (r, θ) grids of size $N_r \times N_\theta = 200 \times 100$ prepared by the conformal map of Appendix B. A sketch of the computational grid (less resolution than used in the simulations) is shown in Fig. 1. Standard second order discretization is used for the spatial derivatives. For the time stepping a second order Runge-Kutta-scheme and a time step $\Delta t=1.0\cdot10^{-8}$ is employed. The Kurganov-Tadmor central semi-discrete scheme is used for the conservative part of the evolution equations [10]. At the targets sheath boundary conditions are imposed, i. e. $\partial n/\partial \theta = 0$ and $u_{\parallel} = \pm c_s$, where $c_s^2 = \sqrt{2T/m_i}$ defines the sound speed. For the outer boundary zero derivatives are assumed for n and u_{\parallel} and at the separatrix the density is prescribed by a constant

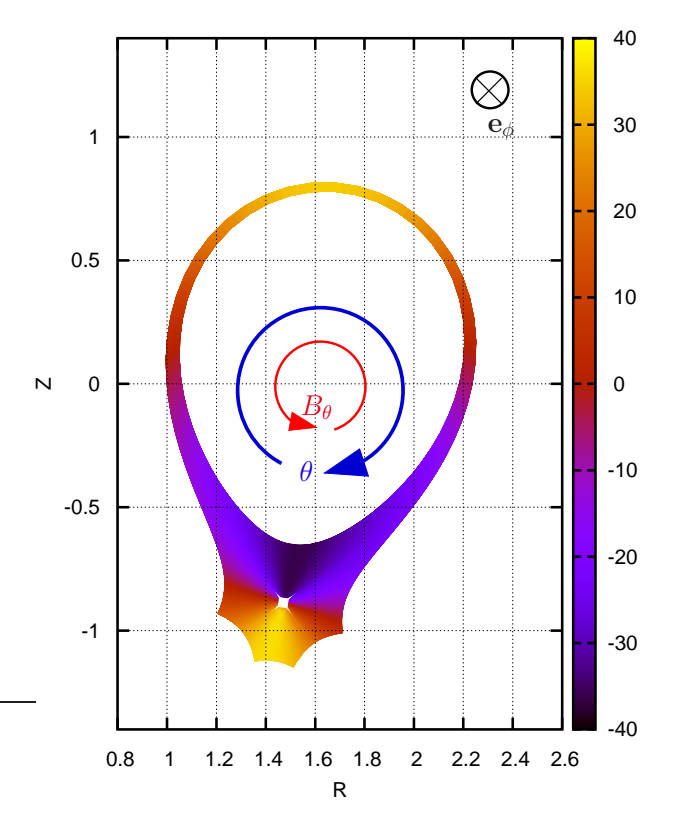


FIG. 2 (Color online) Physical component of the radial component of velocity \mathbf{u}_{\times} defined by Eq. 5 being responsible for advection of particles into and out of the SOL for the model geometry used in this work and sketched in Fig. 1. The arrows and the vector direction symbol give orientation on the direction of increasing angle θ , the sign of the poloidal magnetic field B_{θ} with respect to the angle coordinate direction and the direction of the toroidal basis vector \mathbf{e}_{ϕ} .

value $2 \cdot 10^{19}$ m⁻³, whereas the velocity gradient is set to zero, $\partial u_{\parallel}/\partial r=0$. The time evolution of density n and flow velocity u_{\parallel} is followed until a stationary state is obtained. The parameters chosen were $R_0=1.65$ m, $h{=}1.2$ m, $C{=}0.2785$, $B_0{=}2.5$ T, $T{=}75$ eV and an ion mass $m_i=2$ m_p . The value for C provides a separatrix averaged value $\langle \hat{B}_{\theta} \rangle = -0.28$ T. The rotation angle ξ has been chosen as -0.15. The definition of the geometric quantities r, R_0 , h and ξ is given in the Appendix B. The Fig. 3 shows results for the stationary profiles $n(\theta)$ and $u_{\parallel}(\theta)$ at r=1.002 h, i. e. inside the SOL and close to the separatrix. The corresponding radial profiles of the density n(r) at the inner and outer target and the inner and outer midplane are shown in Fig. 4. The density profile in Fig. 3 shows a pronounced maximum occuring in the central region where the electron drift $-u_{\times}^{r}$ is positive, therefore providing an inflow from the core plasma into the SOL (see Fig. 3 top). The poloidal component of \mathbf{u}_{\times} is more than 2 orders of magnitude smaller than the poloidal projection of sound speed and does not have a significant impact on the parallel flow. The most striking result is the appearance of supersonic flows with Mach number $M=u_{\parallel}/c_s$, $c_s^2=2T/m_i$, being above 1 or less than

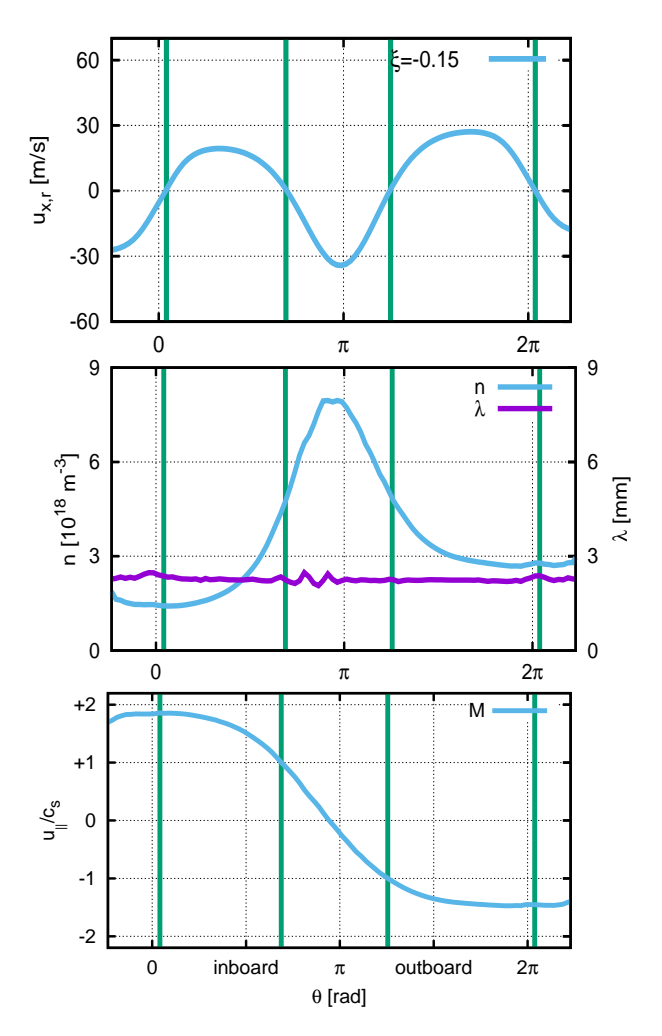


FIG. 3 (Color online) From top to bottom: profiles of the radial physical component of the drift velocity \mathbf{u}_{\times} , the density n and Mach number vs poloidal angle θ for the magnetic field configuration with ξ =-0.15 and at r-h=2.5 mm. The green lines label the points where u_{\times}^{r} =0. Additionally the center plot includes the profile of the decay length Λ given by the numerical values of $|\partial \ln n/\partial r|^{-1}$.

-1 in the velocity profile (Fig. 3 bottom). A very important result of the 2D simulations is an almost exponential decay of the density $n \sim e^{-r/\Lambda}$ with respect to the flux label r and Λ being almost constant along θ inside the SOL and not to close to the separatrix. This is illustrated by the red colored line in the mid figure of Fig. 3 showing $\Lambda = |\partial \ln n/\partial r|^{-1}$ and by the logarithmic plots in Fig. 4 bottom. Right at the separatrix the results are considered as less significant, because the fixed particle density boundary condition there is probably not well suited to get a realistic picture for the inflow/outflow conditions. For this reason the following discussion is restricted to the region r > 1.0021 h, where boundary effects do not play a significant role anymore (this has been proved by the use of different boundary conditions).

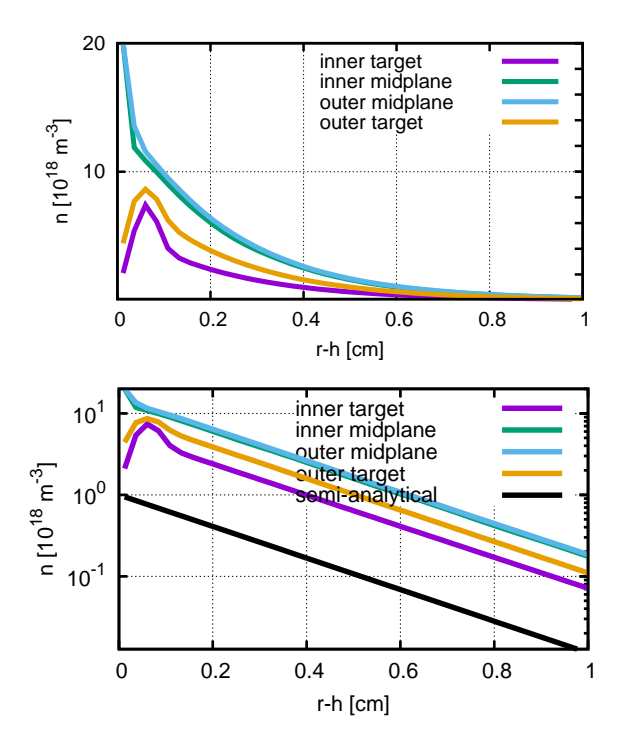


FIG. 4 (Color online) Profiles of density n at the inner and outer target and the inner and outer midplane in linear (top) and logarithmic (bottom) representation. The separatrix is located at $r{=}h$. The black line in the bottom figure is the fitting curve $e^{-r/\Lambda}$ where the averaged value of Λ shown in Fig. 3 is used.

V. 1D MODEL REDUCTION

Justified by the results of the 2D simulation described in the previous section it is assumed that

$$\frac{\partial n}{\partial r} = -\frac{n}{\Lambda} \tag{14}$$

where $\Lambda = \mathrm{const.}$ Note that the physical decay length λ is given by $\lambda = \sqrt{g_{rr}}\Lambda$, where the square root of the metric coefficient g_{rr} determines the flux expansion factor f_x often used in the analysis of scrape-off widths [2]. The flux expansion f_x can be understood as the ratio between the values of $\sqrt{g_{rr}}$ at the target and the outer midplane. Furthermore, the model equations Eqs. 11-12 are simplified by neglecting the poloidal component of the velocity \mathbf{u}_{\times} , any particle sources and the terms due to the parallel variation of B (except in the diamagnetic effects). These assumptions were justified a posteriori by switching off the particular terms in the 2D simulations and proving that the results were not significantly changed. Based on these assumptions the stationary case in EDD-regime is described by a one-dimensional model

$$u_{\parallel} \frac{\partial n}{\partial \theta} = -n \frac{\partial u_{\parallel}}{\partial \theta} - \frac{B}{B^{\theta}} \frac{u_{\times}^{r}}{\Lambda} n \tag{15}$$

$$u_{\parallel} \frac{\partial u_{\parallel}}{\partial \theta} = -\frac{2T}{m_i} \frac{\partial n/\partial \theta}{n} \tag{16}$$

Combining these equations, and using the Mach number $M=u_{\parallel}/c_s$ and the logarithmic density $N=\ln n$ as dependent variables, one obtains

$$(1 - M^2)\frac{\partial M}{\partial \theta} = F, \quad F = -\frac{B}{B^{\theta}} \frac{u_{\times}^r}{\Lambda c_c}$$
 (17)

$$\frac{\partial N}{\partial \theta} = -M \frac{\partial M}{\partial \theta} \tag{18}$$

The solutions of Eqs. 17 and 18 are

$$M - \frac{M^3}{3} = K, \quad K = -\int \frac{B}{B^{\theta}} \frac{u_{\times}^r}{\Lambda c_s} d\theta + C_M$$
 (19)

$$N = -\frac{M^2}{2} + C_N (20)$$

where C_M and C_N are constant. Depending on the particular value of K different solution branches for Eq. 19 and thus bifurcations are possible as illustrated by Fig. 5. Inspection of Eq. 17 shows that the points where the drift velocity u_x^r is zero are of special interest because there $\partial M/\partial\theta=0$ and/or $M=\pm 1$. Thus, if F=0 and $\partial M/\partial\theta$ and $\partial F/\partial\theta$ are finite, a transition occurs to supersonic parallel flow with |M|>1. Differentiation of Eq. 17 gives the following relation valid for such transition points

$$\frac{\partial F}{\partial \theta}\Big|_{|M|=1} = -2M \left(\frac{\partial M}{\partial \theta}\right)^2$$
 (21)

with the consequence that if F=0 and $\partial F/\partial \theta > 0$ at a particular point only a supersonic transition through M=-1 is possible, whereas F=0 together with $\partial F/\partial \theta < 0$ is compatible only with a transition through M=+1. A sit-

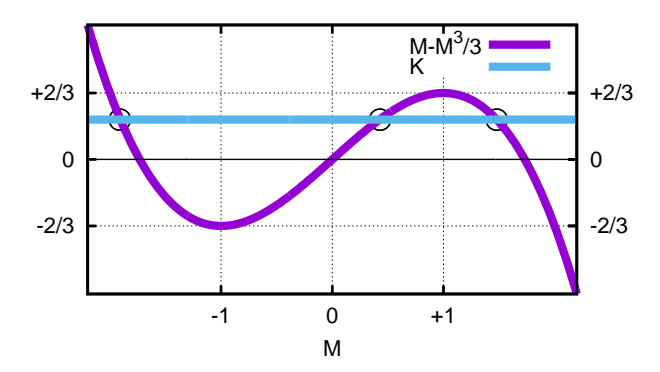


FIG. 5 (Color online) Illustration of a graphical solution of Eq. 19. If |K| < 2/3 three solutions exist (example K = 0.4 labeled by circles). For |K| = 2/3 two solutions exist and for |K| > 2/3 only a single real solution is possible.

uation relevant for the drift-based transport considered in this work is the existence of - at least - two possible transition points where $u_{\times}^{r}=0$ (see Fig. 3 top). This is due to the fact that the diamagnetic flows always introduce both, regions of particle inflow and outflow in

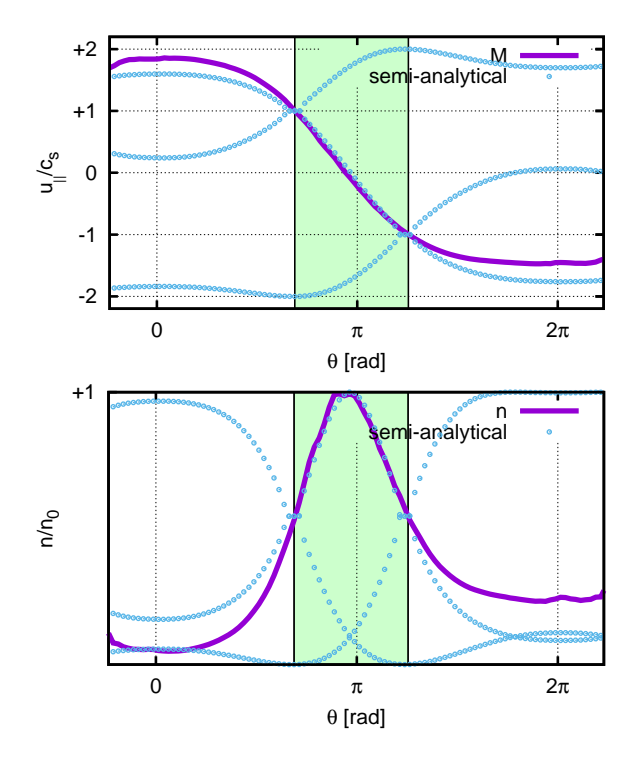


FIG. 6 (Color online) Profiles of Mach number and density vs poloidal angle θ already shown in Fig. 3 but here complemented by the three possible solution branches of Eq. 19. The region between the two transition points is highlighted in green.

the SOL. Requiring $M=\pm 1$ at two consecutive transition points, with u^r_{\times} not changing sign between these points, a conditional equation for the decay length Λ results from Eq. 17

$$\Lambda = \frac{3}{4} \int \left| \frac{B}{B^{\theta}} \frac{u_{\times}^{r}}{c_{s}} \right| d\theta \tag{22}$$

The integral is taken from one transition point to the next one. This situation with two consecutive transition points corresponds to the result for the Mach number M shown in Fig. 3 bottom, where the green lines label the special points where $u_{\times}^{r}=0$. Using Eq. 22 the solution branches of Eq. 19 can be calculated. The possible solutions for |M|=1 appearing at two points along the magnetic field line are sketched in Fig. 6 by three dotted lines and compared with the results from the 2D simulations of Fig. 3. In the 2D simulations the system picks a certain solution which follows closely the smooth solution branch of Eq. 19 connecting the points of supersonic transition. Also the density profile agrees well with the result $n\sim e^{-M^2/2}$. The agreement is optimal for the region between the two transition points, where the particles are pushed across the sparatrix into the SOL (highlighted in green in Fig. 6). Outside this region the agreement is not as good, but still the 1D result gives a good qualitative description of the solution found in the detailed 2D simulation. Therefore, the analysis of the 1D reduced model explains the supersonic flows in the results presented for

the EDD-regime above. Of course, not all features can be covered by the 1D consideration, in particular because the assumption of a constant Λ is not always justified for different magnetic field configurations. However, the basic features of the profiles found by 2D simulations are very well understood in the light of the analysis of the simplified 1D model and, therefore, it provides a good approximation for semi-analytical considerations. Finally, it should be noted that for cylindrical geometry the integral in Eq. 22 can be estimated via

$$u_{\times}^{r} \approx \frac{2T}{eBR_{0}}\cos\theta, \quad B^{\theta} \approx \frac{\hat{B}_{\theta}}{a}$$
 (23)

where a is the minor radius and \hat{B}_{θ} the physical component of the poloidal magnetic field. Integration for $\pi/2 \le \theta \le 3\pi/2$ gives for the scrape-off width

$$\Lambda = \frac{3aT}{e\hat{B}_{\theta}R_{0}c_{s}} \tag{24}$$

and this result is - despite a factor of 4/3 - identical with Goldston's estimate for λ for singly charged ions and atomic mass of 2 (Eq. 1 in [1]). Thus, the assumption of supersonic transitions in the fluid model considered here offers an alternative derivation of Goldston's estimate for the scrape-off width.

VI. 2D SIMULATIONS IN X-POINT GEOMETRY FOR ION DIAMAGNETIC DRIFT DOMINATED TRANSPORT

In this section the exercise of Sec. IV is repeated, but for the regime dominated by the ion diamagnetic drift (denoted by IDD-regime in Appendix A). At this point it is important to note that the simple expression Eq. 22 - and even more the estimate Eq. 24 - giving a quick estimate for the SOL width and building a bridge to Goldston's approach has to be used with care. To illustrate the subtleties an example of 2D simulations and the related 1D approximation is discussed here where the same parameters are used to obtain the results of Figs. 3, 4 and 6, but with plus-sign in Eqs. 1 and 11, i. e. switching from EDD- to IDD-regime. The results analogous to Fig. 3 are shown in Fig. 7. The density and Mach number profiles shown in the center bottom figure are very different to the case discussed above. Now two maxima appear in the density profile, corresponding to the particle feeding in the two regions with $u_{\times}^{r}>0$ and the velocity profile shows a jump in the center region close to $\theta = \pi$. In this case supersonic transitions occur, but at different locations, and also a minimum, i. e. $\partial M/\partial \theta = 0$, appears at a point with $u_{\times}^{r}=0$. The most important differences with respect to the estimates discussed above is the smaller value for Λ found in the 2D simulations (the red curve in the center plot) and the appearance of a bifurcational shock wave like structure becoming manifest in the discontinuous jump of the Mach number. A closer inspection of these results shows that this reduced

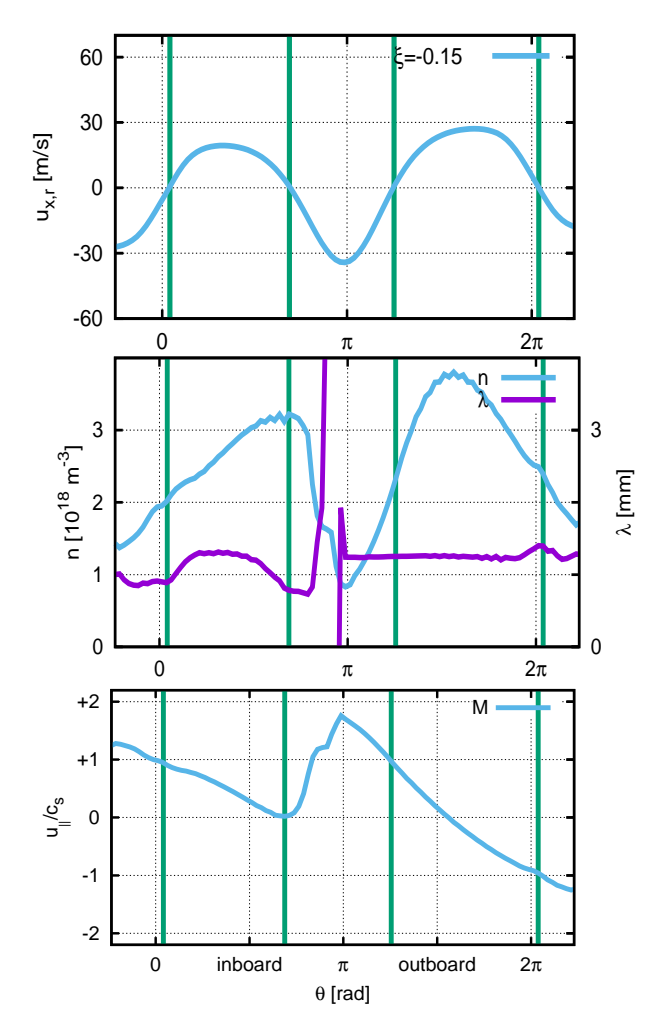


FIG. 7 (Color online) Simulation for the parameters chosen for Fig. 3 but for the ion diamagnetic drift dominated regime. From top to bottom: profiles of the radial physical component of the drift velocity \mathbf{u}_{\times} , the density n and Mach number vs poloidal angle θ for the magnetic field configuration with ξ =-0.15. The green lines label the points where u_{\times}^{r} =0. Additionally the center plot includes the profile of the decay length Λ given by the numerical values of $|\partial \ln n/\partial r|^{-1}$.

SOL width in the outboard region ($\Lambda=1.23$ mm instead of $\Lambda=2.24$ mm in the case discussed above) can be related again to Eq. 22 but now for the points at θ =3.94 and θ =6.40 connecting two supersonic transitions. It might be speculated that the inflow regions with $u_{\times}^{r}>0$ determine the velocity profile and therefore transition points and SOL width Λ . On the other hand, the discontinuity in M can be explained by a bifurcation forced by the constraint given by Eq. 17 constraining the parallel flow to $\partial M/\partial \theta = 0$ and/or $M = \pm 1$ at the points where the drift velocity u_x^r is zero. But, the reason why the dynamical system is choosing $\partial M/\partial \theta = 0$ at one point and not |M| = 1is not clear up to now. This example demonstrates that the details of the X-point geometry have a significant impact on the SOL width, which is not taken into account in a formula like Eq. 24. Also a significant difference is

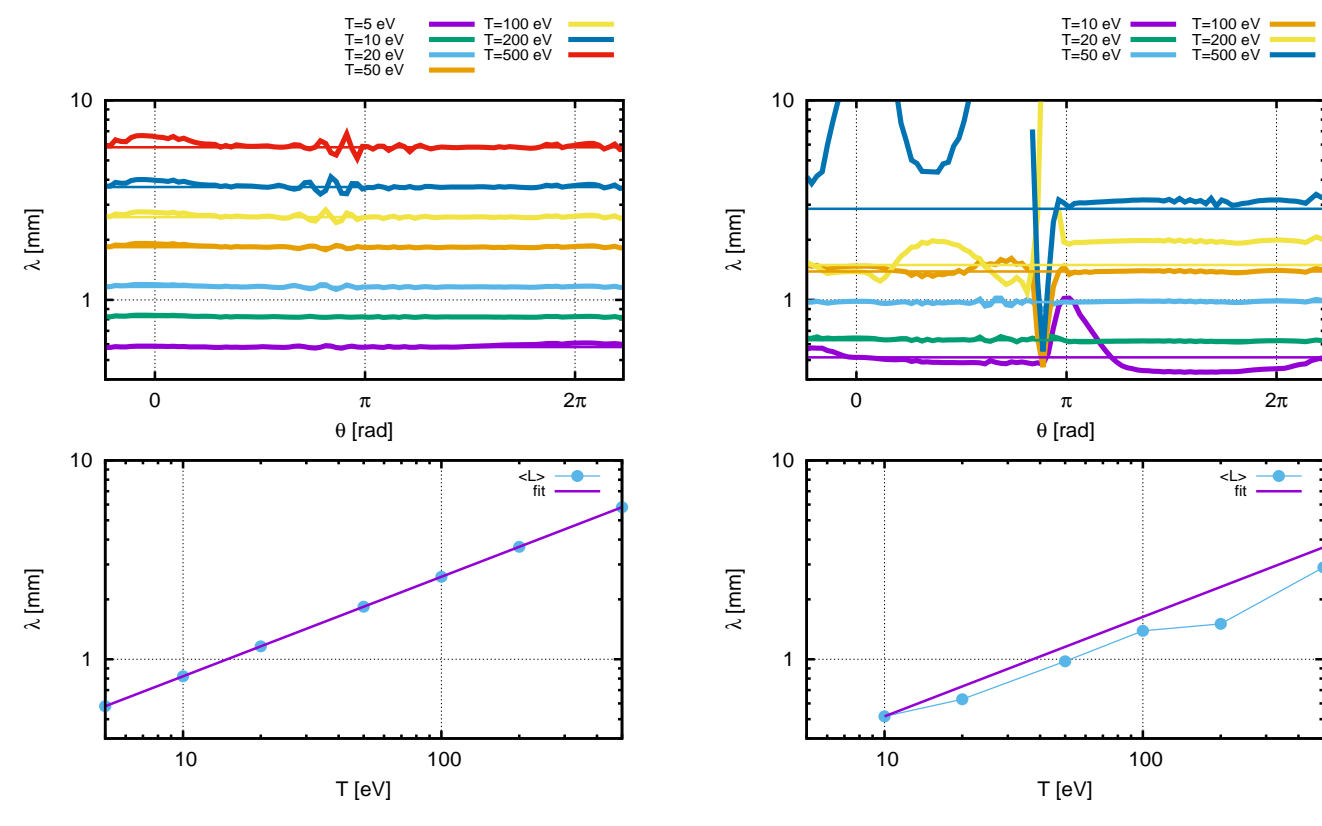


FIG. 8 (Color online) Top: Dependence of Λ on the electron temperature T_e in electron drift dominated regime. Shown are the profiles of the inverse logarithmic derivatives $\Lambda = |\partial \ln n/\partial r|^{-1}$ overlaid by straight lines representing the poloidal averages. Bottom: Log-Log-plot to prove the parametric dependence according to Eq. 22. for Λ .

FIG. 9 (Color online) Top: Dependence of Λ on the electron temperature T_e in ion drift dominated regime. Shown are the profiles of the inverse logarithmic derivatives $\Lambda = |\partial \ln n/\partial r|^{-1}$ overlaid by straight lines representing the poloidal averages. Bottom: Log-Log-plot to prove the parametric dependence according to Eq. 22. for Λ .

apparent between the IDD- and EDD-regime. A particle inflow from the SOL to core in the upper region opposite to the X-point seems to separate the inboard and outboard region leading to shock wave like structures also causing certain numerical uncertainties like problems in finding a stationary state. It must be stressed that the 1D reduced model derived here has been confirmed a posteriori using the numerical 2D findings especially for the EDD-regime. But, for an extended discussion also the principal mechanism for the Mach number profile to fulfill the general condition Eq. 17 must be known to get a more quantitative picture. However, in the next section it is shown basic parametric dependencies of Eq. 22 prevail for both, the electron drift dominated regime and the ion drift dominated regime.

VII. SOL WIDTH IN PARAMETER SCAN

In this section results from 2D simulations are presented to examine whether the details of the X-point geometry have some effect on the basic relations $\Lambda \sim T^{1/2}$ and $\Lambda \sim \hat{B}_{\theta}^{-1}$ expressed in Goldston's estimate and how it is affected by the different regimes. Several simulations

have been conducted for the ASDEX like geometry with parameters chosen as in Section IV and VI, and firstly for varying temperatures 5 eV $\leq T \leq$ 500 eV and secondly for varying poloidal magnetic field, i. .e. varying value of C in a range such that 0.028 T $\leq \langle \hat{B}_{\theta} \rangle \leq 0.56$ T. The results for the profiles of the decay length $|\partial \ln n/\partial r|^{-1}$ are shown in logarithmic plots Figs. 8-11. It can be seen that in the EDD-regime (Figs. 8 and 10) the decay length obtained by the logarithmic derivative of the numerical profiles of the density in the SOL is to a large extent constant along the poloidal angle. Also it is obvious that the values of Λ follow closely the expected functional dependence on T and \hat{B}_{θ} described by Eq. 22. However, in some cases the precise values of Λ can differ by a factor of 2-4 for inner and outer target and with respect to the analytical result from Eq. 22, especially for low $\langle \hat{B}_{\theta} \rangle$. The situation looks much more complicated for the IDDregime (Figs. 9 and 11). There the poloidal variation of the decay length can be strong, in particular when the drift effect becomes stronger for higher temperatures and lower poloidal field. However, the parametric dependence of the averaged decay length on T and B_{θ} agrees quite well with the Goldston like formula Eq. 22. In summary it can be concluded that the numerical results confirm the

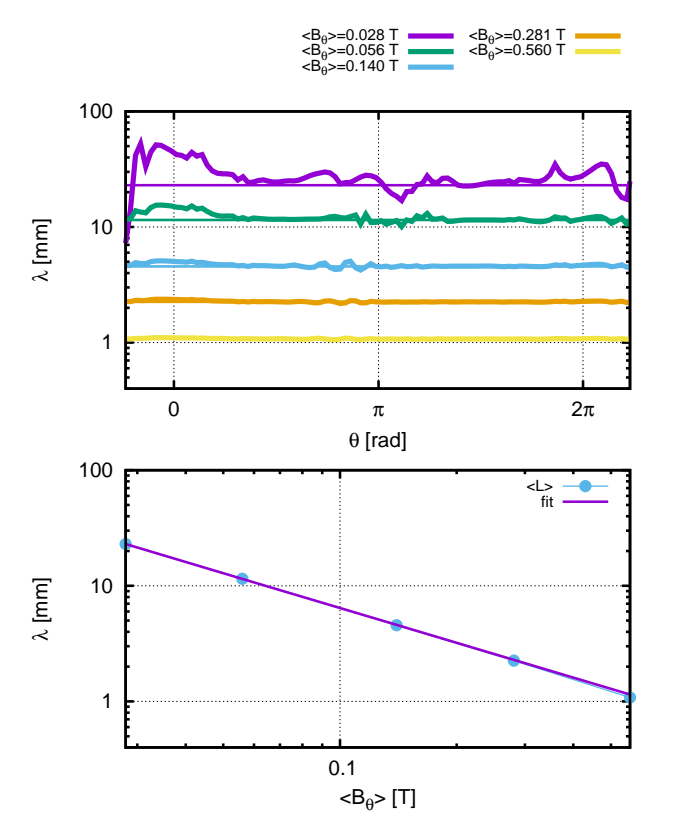


FIG. 10 (Color online) Top: Dependence of Λ on the poloidal magnetic field \hat{B}_{θ} in electron drift dominated regime. Shown are the profiles of the inverse logarithmic derivatives $\Lambda = |\partial \ln n/\partial r|^{-1}$ overlaid by straight lines representing the poloidal averages. Bottom: Log-Log-plot to prove the parametric dependence according to Eq. 22. for Λ .

linear functional dependance of the averaed decay length on the poloidal Larmor radius ρ_p

$$\langle \Lambda \rangle \sim \rho_p, \quad \rho_p = \sqrt{\frac{2Tm_i}{e^2 \hat{B}_\theta^2}}$$
 (25)

but uncertainties remain concerning the proportionality constant and in some cases the assumption of an overall constant decay length is not justified. However, for most of the cases considered the expression Eq. 22 gives a very precise estimate for the SOL width found in the 2D simulations.

VIII. DIFFUSIVE TRANSPORT AND SOL WIDTH

In this section 2D results from simulations including homogeneous diffusive particle feeding of the SOL are presented. For this purpose the model equations Eq. 1 and 11 are modified as follows (again the minus sign is used for the EDD-regime)

$$\frac{\partial n}{\partial t} + \nabla \cdot (n\mathbf{u}_{\parallel}) - \nabla \cdot (n\mathbf{u}_{*}) = \nabla \cdot (\mathbf{D}_{\perp} \cdot \nabla n)$$
 (26)

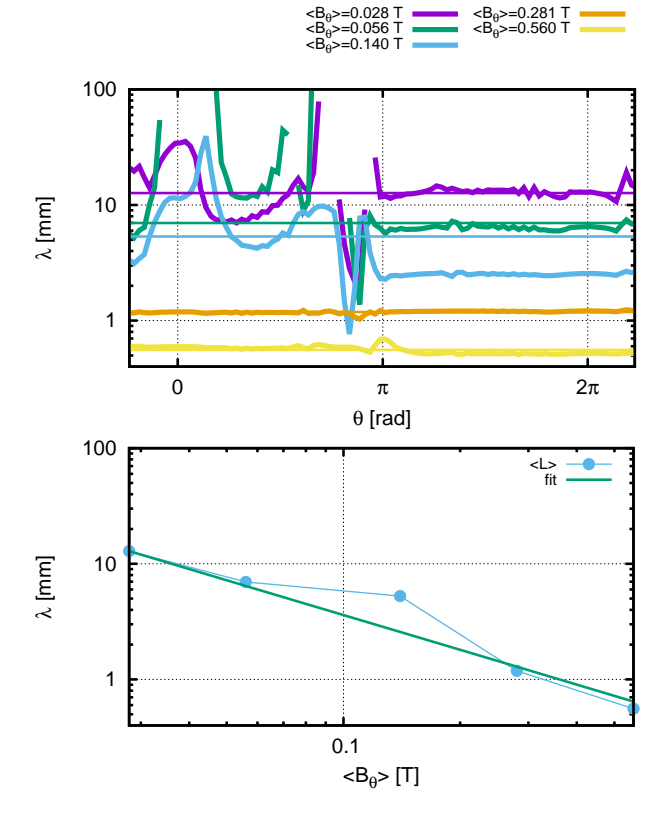


FIG. 11 (Color online) Top: Dependence of Λ on the poloidal magnetic field \hat{B}_{θ} in ion drift dominated regime. Shown are the profiles of the inverse logarithmic derivatives $\Lambda = |\partial \ln n/\partial r|^{-1}$ overlaid by straight lines representing the poloidal averages. Bottom: Log-Log-plot to prove the parametric dependence according to Eq. 22. for Λ .

$$\frac{\partial n}{\partial t} + \frac{1}{J} \frac{\partial}{\partial \theta} \left(J \frac{B^{\theta}}{B} n u_{\parallel} - J n u_{\times}^{\theta} \right) - \frac{1}{J} \frac{\partial}{\partial r} \left(J n u_{\times}^{r} \right)$$

$$= \frac{1}{J} \frac{\partial}{\partial r} \left(J \frac{D_{\perp}}{q_{rr}} \frac{\partial n}{\partial r} \right)$$
(27)

Here D_{\perp} is a constant diffusion coefficient. The results for varying values of D_{\perp} in the range between 0.001 m²/s and $0.5 \text{ m}^2/\text{s}$ are shown in Figs. 12 and 13. Again the profiles of the inverse logarithmic derivative of the density are shown. For the EDD-regime and low values of D_{\perp} the profiles are rather flat but for higher values of D_{\perp} the assumption of a constant Λ is not justified anymore. For the IDD-regime the same strong variations of decay length are visible as in the previous sections. For further analysis also the averaged values of the numerically obtained decay length are shown as straight horizontal lines in Figs. 12 and 13 top. These are complemented by log-log-plots including a fit based on the functional $\Lambda = \Lambda_0 \left(1 + \sqrt{1 + D_{\perp}/D_*} \right) / 2$. which is motivated by an extension of the 1D model we will introduce below. Despite the details of decay length profiles it is obvious that additional diffusion increases the SOL width and Λ changes significantly for $D_{\perp}>0.01 \text{ m}^2/\text{s}$. For $D_{\perp}=0.2$ m^2/s it is about a factor of 5 larger than the drift-based value for both regimes. Using the same assumptions as

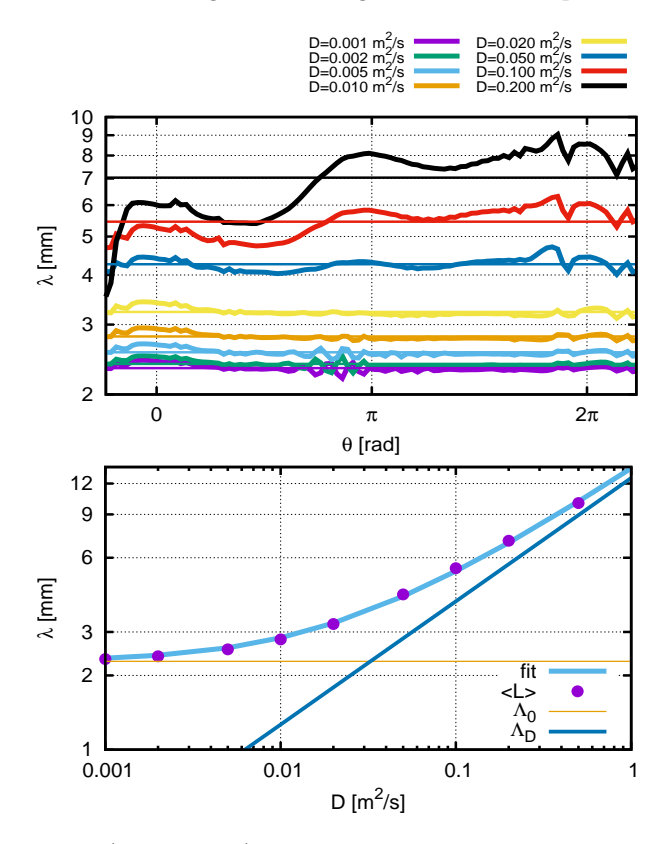


FIG. 12 (Color online) Electron drift dominated regime. Top: Dependence of Λ on the additional particle diffusion characterized by D_{\perp} . Shown are the profiles of the inverse logarithmic derivatives $\Lambda = |\partial \ln n/\partial r|^{-1}$ overlaid by straight lines representing its respective θ -averaged value. Bottom: Loglog-plot of decay length vs diffusion coefficient compared to the fitting formula Eq. 33 and the limiting cases Λ_0 and Λ_D .

in Section V we incorporate the particle diffusion by the following extension of Eq. 15

$$u_{\parallel} \frac{\partial n}{\partial \theta} = -n \frac{\partial u_{\parallel}}{\partial \theta} + \frac{B}{B^{\theta}} \left(-\frac{u_{\times}^{r}}{\Lambda} + \frac{D_{\perp}}{\Lambda^{2} q_{rr}} \right) n \tag{28}$$

and the equation for the Mach number M becomes

$$M - \frac{M^3}{3} = \int \frac{B}{B^{\theta}} \left(-\frac{u_{\times}^r}{\Lambda c_s} + \frac{D_{\perp}}{\Lambda^2 g_{rr} c_s} \right) d\theta + C_M$$
 (29)

Therefore, a quadratic equation for Λ results

$$c_2 \Lambda^2 - c_1 \Lambda - c_0 D_{\perp} = 0 \tag{30}$$

where

$$c_2 = M_2 - \frac{M_2^3}{3} - M_1 + \frac{M_1^3}{3} \tag{31}$$

and

$$c_1 = -\int_{\theta_1}^{\theta_2} \frac{Bu_{\times}^r}{B^{\theta}c_s} d\theta, \quad c_0 = \int_{\theta_1}^{\theta_2} \frac{B}{B^{\theta}g_{rr}c_s} d\theta$$
 (32)

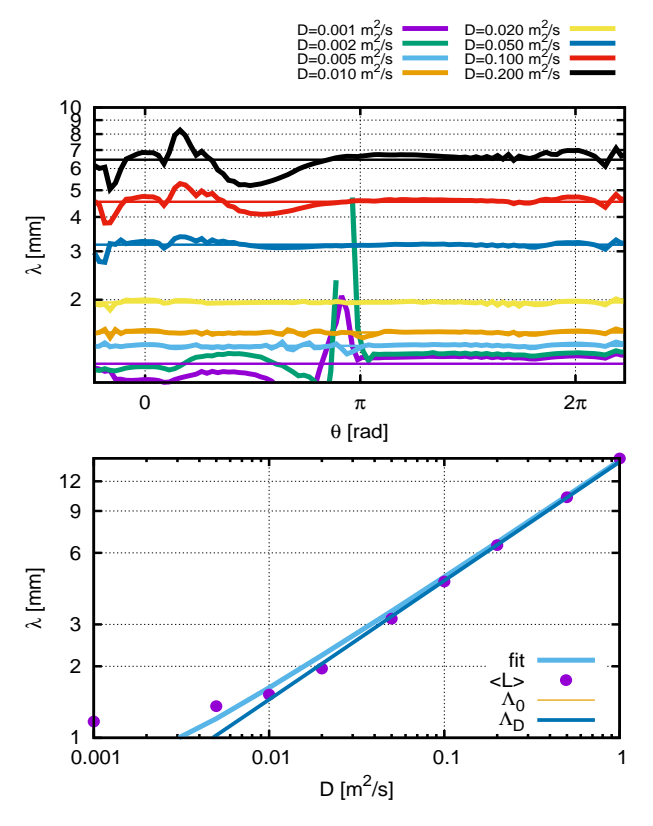


FIG. 13 (Color online) Ion drift dominated regime. Top: Dependence of Λ on the additional particle diffusion characterized by D_{\perp} . Shown are the profiles of the inverse logarithmic derivatives $\Lambda = |\partial \ln n/\partial r|^{-1}$ overlaid by straight lines representing its respective θ -averaged value. Bottom: Log-log-plot of decay length vs diffusion coefficient compared to the fitting formula Eq. 33 and the limiting cases Λ_0 and Λ_D .

Here $M_1=M(\theta_1)$ and $M_2=M(\theta_2)$ are the Mach numbers at the integration boundaries. The problem in solving equation Eq. 30 is the lack of appropriate integration limits θ_1 and θ_2 . In Section V the transition points with |M|=1 offered a reasonable choice. For the drift-diffusive problem of Eq. 29 such a choice is not obvious. However, the solution of Eq. 30 can be written in the form

$$\Lambda = \frac{\Lambda_0}{2} \left(1 + \sqrt{1 + \frac{D_\perp}{D_\perp^*}} \right) \tag{33}$$

with Λ_0 the decay length in drift limit $(D_{\perp}=0)$ and D_{\perp}^* a scaling diffusion coefficient

$$\Lambda_0 = \frac{c_1}{c_2}, \quad D_\perp^* = \frac{c_1^2}{4c_0c_2}$$
(34)

For $D_{\perp}\gg D_{\perp}^*$ the decay length is given by

$$\Lambda = \Lambda_D = \frac{\Lambda_0}{2} \sqrt{\frac{D_\perp}{D_\perp^*}} = \sqrt{\frac{4D_\perp c_0}{c_2}} \tag{35}$$

and the contribution c_1 due to the drift effect is canceled out. This gives reason to the particular fit function

used in Figs. 12 and 13. resulting in Λ_0 =2.27 mm and $D_*=8.08\cdot10^{-3} \text{ m}^2/\text{s}$ for the EDD-regime. Even though the decay lengths in the IDD-regime, Fig. 13, show a similar tendency, the fit function does not work as well as for the EDD-regime. This reflects the more irregular profiles of the decay lengths already seen in the previous sections. It can be concluded that even a particle diffusion of D_{\perp} =0.05 m²/s, which is relatively low compared to typical edge transport simulations, is enough to cover the effects of drift-based transport and its related SOL width completely. This is of importance for future studies with more sophisticated numerical approaches like the one reported in Ref. [4]. Also the existence of transition points located at u_{\times}^{r} =0 might give a hint for experimental proof of the dominance of the drift-based particle transport underlying the heuristic model of Goldston. To extend the discussions on the particularities and in view of the results of Ref. [4] we show in Fig.14 additional Mach number profiles for the IDD-regime and for varying diffusivity $0.001 \text{ m}^2\text{s}^{-1} \le D_{\perp} \le 0.1 \text{ m}^2\text{s}^{-1}$. It is apparent that the shock wave like structure, i. e. the sudden jump in Mach number, and supersonic flows disappear for $D_{\perp}>0.01~\rm m^2s^{-1}$ and only a single stagnation point with M=0 remains. It is noteworthy that the authors of Ref. [4] report about numerical diffulties for values D_{\perp} <0.1 m²s⁻¹. Possibly, these are related to the shock wave signatures observed in this work and a more detailed comparison with Mach number profiles might confirm this.

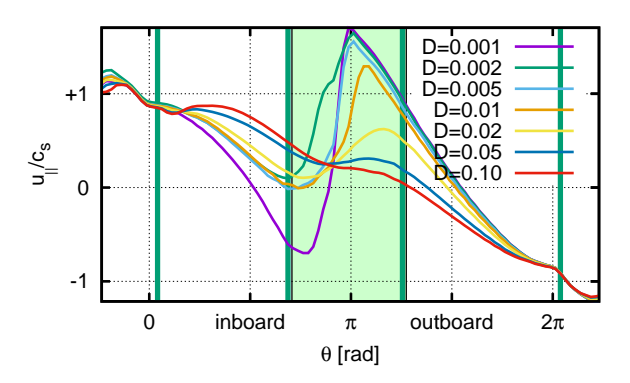


FIG. 14 (Color online) Mach number profiles in the IDD-regime for varying diffusion coefficient. The green lines label the points where $u_x^r = 0$.

IX. CONCLUSIONS

- The parametric dependence of Goldston's estimate for the scrape-off particle width has been assessed by 2D simulations in X-point magnetic configurations supported by a 1D approximative model. The functional dependencies of Goldston's λ -formula have been confirmed for the averaged density decay length.
- The simulations indicate that in situations where the radial particle transport in the SOL is dominated by

the diamagnetic drift effect supersonic transitions are likely to occur. On the other hand, the particular location for such a transition to occur is inevitably connected with the points where the radial drift is zero in case the drift-based transport is dominant. This differs completely from the diffusion dominated case and might give a hint for experimental proof.

- The inverse \hat{B}_{θ} dependence is confirmed but for a quantitative calculation of the scrape-off width it is of importance to use the local value in the region of particle inflow from the core into the SOL to get the right proportionality factor.
- The different regimes where either the electron diamagnetic drift or the ion diamagnetic drift dominate the perpendicular transport show very different signatures. The first shows a much more simple overall structure of density and flow profiles, which can be described quite well by a reduced 1D model. The latter exhibits shock wave signatures at the top of the standard ASDEX Upgrade magnetic configuration considered in this work and strong variations in the radial density profiles.
- An additional particle diffusion increases the decay length Λ significantly even for moderate diffusivities compared to typical values used for anomalous diffusion in transport codes. Therefore, studies on the drift-based effects should be pushed to the numerically more challenging limit of very small particle diffusion in the range of $D_{\perp} \sim 10^{-2}$ m²/s and beyond.
- Finally, we point out that the relevance of an assumed dominance of diamagnetic drifts in the perpendicular particle transport is to be assessed with respect to the quasineutrality constraint as discussed in Appendix A to get more insight into the conditions compatible with the model considered in this work.

Acknowledgments

This work has been carried out within the framework of the EUROfusion Consortium and has received funding from the Euratom research and training programme 2014-2018 under grant agreement No 633053. The views and opinions expressed herein do not necessarily reflect those of the European Commission.

References

- $[1]\ R.\ J.\ Goldston,\ Nucl.\ Fusion\ 52,\ 013009,\ 2012$
- [2] T. Eich et al., Nucl. Fusion 53, 093031, 2013
- [3] M. Faitsch et al., Plasma Phys. Control. Fusion 57, 075005, 2015
- [4] E. T. Meier et al., Plasma Phys. Control. Fusion 58, 125012, 2016
- [5] V. A. Rozhansky et al., Nucl. Fusion 41, 387, 2001
- [6] T. D. Rognlien et al., J. Nucl. Mat. 266-269, 654-659, 1999

- [7] 'Plasma Confinement' by R. D. Hazeltine and J. D. Meiss, Dover Books on Physics (2003)
- [8] D. Reiser, Phys. Plasmas 19, 072317, 2012
- [9] B. Sieglin et al., Plasma Phys. Control. Fusion 58, 055015, 2016
- [10] A. Kurganov and E. Tadmor, J. Comp. Phys. 160, 241-282, 2000

APPENDIX A: Diamagnetic currents and quasineutrality

As mentioned in Sec. II the model proposed by Eqs. 1 and 2 have to be considered with caution. Due to the quasineutrality condition $\nabla \cdot \mathbf{J} = 0$, in principle it does not make a difference whether one uses the electron or ion continuity equation to describe the evolution of particle density. However, the deliberate reduction of the particle flow to a drift-dominated scenario as in Eq. 1 introduces limitations for the applicability of the model with respect to parallel currents, sources and sinks and electric fields. A general study or conclusion on this issue it out of the scope of this work. But, in this section we try to discuss briefly a few important implications of the fluid model of Sec. II.

To elucidate the interplay of parallel and perpendicular currents we start with the general expression for perpendicular the flow velocity \mathbf{V}_{\perp} of a species with charge number Z (see, e. g. Ref.[8])

$$\mathbf{V}_{\perp} = \frac{\mathbf{E} \times \mathbf{B}}{B^{2}} + \frac{\mathbf{B} \times \nabla p}{ZenB^{2}} + \frac{m}{ZeB^{2}} \mathbf{B} \times \frac{d\mathbf{V}}{dt} + \frac{\mathbf{S}_{m} \times \mathbf{B}}{ZenB^{2}} + \frac{mS_{n}}{ZenB^{2}} \mathbf{B} \times \mathbf{V}_{\perp}$$
(A1)

where $d/dt = \partial/\partial t + \mathbf{V} \cdot \mathbf{\nabla}$ and S_m include sources, sinks and viscosity for particles and momentum. Using this recursive expression for the ion-electron plasma considered here and taking into account quasineutrality $\mathbf{\nabla} \cdot \mathbf{J} = 0$ one finds the relations

$$\nabla \cdot (n\mathbf{v}) = \nabla \cdot (n\mathbf{u})$$

$$= \nabla \cdot (n\mathbf{v}_{\parallel} + n\mathbf{v}_{*}) + \nabla \cdot (n\mathbf{V}_{E})$$

$$-\nabla \cdot \left(\frac{m_{e}n}{eB^{2}}\mathbf{B} \times \frac{d\mathbf{v}}{dt} + \frac{\mathbf{S}_{m}^{e} \times \mathbf{B}}{eB^{2}} + \frac{m_{e}S_{n}^{e}}{eB^{2}}\mathbf{B} \times \mathbf{v}_{\perp}\right)$$

$$= \nabla \cdot (n\mathbf{u}_{\parallel} + n\mathbf{u}_{*}) + \nabla \cdot (n\mathbf{V}_{E})$$

$$+\nabla \cdot \left(\frac{m_{i}n}{eB^{2}}\mathbf{B} \times \frac{d\mathbf{u}}{dt} + \frac{\mathbf{S}_{m}^{i} \times \mathbf{B}}{eB^{2}} + \frac{m_{i}S_{n}^{i}}{eB^{2}}\mathbf{B} \times \mathbf{u}_{\perp}\right)$$
(A2)

where \mathbf{u} and \mathbf{v} are the ion and electron flow velocity, respectively. Here \mathbf{u}_* and \mathbf{v}_* denote the diamagnetic drift velocities of ions and electrons, and \mathbf{V}_E is the $E \times B$ -drift velocity. The terms proportional to $d\mathbf{u}/dt$ and $d\mathbf{v}/dt$ are the respective inertial contributions (polarisation drifts).

Of course, these relations are just a variant of the general perpendicular momentum equations, telling nothing more that the plasma flows, sources, sinks and electric fields have to rearrange in a way that quasineutrality is retained. A general treatment of this situation is a complicated task, even numerically. However, in accordance with the neglect of sources, sinks and viscosity in the discussions of this work and in Ref. [1] we distinguish two different regimes dominated by diamagnetic drifts:

Electron diamagnetic drift regime (**EDD-regime**): the radial particle transport is determined by the electron diamagnetic drift \mathbf{v}_*

$$\nabla \cdot (n\mathbf{v}) = \nabla \cdot (n\mathbf{v}_{\parallel} + n\mathbf{v}_{*}) \tag{A3}$$

which requires

$$\nabla \cdot \left(n\mathbf{V}_E - \frac{m_e n}{eB^2} \mathbf{B} \times \frac{d\mathbf{v}}{dt} \right) = 0$$
 (A4)

Ion diamagnetic drift regime (**IDD-regime**): the radial particle transport is dominated by the ion diamagnetic drift \mathbf{u}_*

$$\nabla \cdot (n\mathbf{u}) = \nabla \cdot (n\mathbf{u}_{\parallel} + n\mathbf{u}_{*}) \tag{A5}$$

which requires

$$\nabla \cdot \left(n\mathbf{V}_E + \frac{m_i n}{eB^2} \mathbf{B} \times \frac{d\mathbf{u}}{dt} \right) = 0$$
 (A6)

This means that the SOL model considered here needs the polarisation current of the electrons or ions to close the current loops in the presence of diamagnetic drifts. One might proceed by assuming dominance of the $E \times B$ drift and considering the stationary case giving

$$\mathbf{B} \times \frac{d\mathbf{v}}{dt} \approx \mathbf{B} \times (\mathbf{v}_{\parallel} + \mathbf{V}_{E}) \cdot \nabla \mathbf{V}_{E}$$
 (A7)

$$\mathbf{B} \times \frac{d\mathbf{u}}{dt} \approx \mathbf{B} \times \left(\mathbf{u}_{\parallel} + \mathbf{V}_{E}\right) \cdot \nabla \mathbf{V}_{E} \tag{A8}$$

Inserting these approximations into Eqs. A4 or A6 then would provide an equation for the electric field necessary for quasineutrality in the respective regime. Even for this approximative treatment a non-linear equation for E results which is coupled to the parallel flows of ions and electrons. In this work we did not attempt to solve the full problem connected with the detailed current balance and restrict ourselves to scenario (1). Also, we did not attempt to quantify the consequences of this choice to avoid a chain of additional speculations. Therefore, the comparison of the results presented here with experiments or extended simulations should be accompanied by a detailed analysis of the full drift dynamics including electric fields and currents. Discussions related to these different regimes also can be found in Refs. [1] and [4] and the brief comment of this Appendix gives hints for a systematic assessment of the model used.

APPENDIX B: Magnetic field configuration and conformal mapping

A conformal map $R + iZ = f(r, \theta)$ is defined where R and Z are related to Cartesian coordinates via

$$x = R\cos\phi, \quad y = R\sin\phi, \quad z = Z$$
 (B1)

and f is chosen as

$$f = \left(R_0 - e^{-i\vartheta} \sqrt{r^2 - h^2 e^{2i\vartheta}}\right) e^{i\xi}$$

$$+ \left(1 - e^{i\xi}\right) \left(R_0 + iZ_0\right)$$
(B2)

The coordinate θ is given as a function of θ

$$\vartheta = \frac{\pi}{2\operatorname{erf}(3\pi/s)} \left[\operatorname{erf}\left(\frac{3\pi}{s}\right) - \operatorname{erf}\left(\frac{3\pi - \theta}{s}\right) + \operatorname{erf}\left(\frac{\pi + \theta}{s}\right) - \operatorname{erf}\left(\frac{\pi - \theta}{s}\right) \right]$$
(B3)

The Eqs. B1-B3 define the transformation between the coordinate functions (x, y, z), (R, ϕ, Z) and (r, θ, ϕ) . Due to the properties of conformal maps the coordinates (r, θ, ϕ) are right-handed orthogonal. Their coordinate

lines are similar to tokamak X-point geometries with X-point being located at $r\!=\!h$ and $\theta\!=\!0$. This mapping of an X-point tokamak field onto an orthogonal grid in the (r,θ) -plane is particularly suitable for numerical approaches. Note that for $h\!\to\!0$, $\partial\vartheta/\partial\theta\!=\!1$, a circular geometry is recovered. The parameters R_0 , Z_0 , ξ and s are introduced to translate and rotate the grid and to control the resolution close to the X-point. The point (R_0,Z_0) defines the center of rotation in the (R,Z)-plane and ξ denotes the rotation angle. A parameter $s\!>\!1$ is used to increase the density of grid points close to the X-point while the grid points are still equidistant on the θ -coordinate lines. An example of a resulting grid is shown in Fig. 1. The tranformation is characterized by the Jacobian $J\!=\!\mathbf{e}_r\cdot\mathbf{e}_\theta\times\mathbf{e}_\phi$

$$J = \frac{R}{r} \frac{\partial \theta}{\partial \theta} \frac{r^4}{\sqrt{r^4 - 2h^2 r^2 \cos 2\theta + h^4}}$$
 (B4)

and the metric coefficients g_{rr} , $g_{\theta\theta}$ and $g_{\phi\phi}$

$$g_{rr} = \frac{J}{rR} \frac{1}{\partial \vartheta / \partial \theta}, \quad g_{\theta\theta} = \frac{rJ}{R} \frac{\partial \vartheta}{\partial \theta}, \quad g_{\phi\phi} = R^2$$
 (B5)